AGU PUBLICATIONS

Global Biogeochemical Cycles

RESEARCH ARTICLE
10.1002/2015GB005308

When can ocean acidification impacts be detected from decadal alkalinity measurements?

B. R. Carter[1,2], T. L. Frölicher[3], J. P. Dunne[4], K. B. Rodgers[5], R. D. Slater[5], and J. L. Sarmiento[5]

[1]Joint Institute for the Study of the Atmosphere and Ocean, Seattle, Washington, USA, [2]NOAA Pacific Marine Environmental Laboratory, Seattle, Washington, USA, [3]Environmental Physics, Institute of Biogeochemistry and Pollutant Dynamics, ETH Zürich, Zürich, Switzerland, [4]NOAA Geophysical Fluid Dynamics Laboratory, Princeton University, Princeton, New Jersey, USA, [5]Atmospheric and Oceanic Sciences Program, Princeton University, Princeton, New Jersey, USA

Key Points:
- OA-related alkalinity trend detection is complicated by freshwater cycling variability
- OA-related alkalinity trends are detected earlier using salinity-normalized alkalinity than when using alkalinity
- OA impacts on alkalinity could be detectable across the subtropical gyres by 2030

Supporting Information:
- Data Set S1
- Data Set S2

Correspondence to:
B. R. Carter,
brendan.carter@noaa.gov

Citation:
Carter, B. R., T. L. Frölicher, J. P. Dunne, K. B. Rodgers, R. D. Slater, and J. L. Sarmiento (2016), When can ocean acidification impacts be detected from decadal alkalinity measurements?, *Global Biogeochem. Cycles*, *30*, 595–612 doi:10.1002/2015GB005308.

Received 16 OCT 2015
Accepted 13 APR 2016
Accepted article online 18 APR 2016
Published online 30 APR 2016

Abstract We use a large initial condition suite of simulations (30 runs) with an Earth system model to assess the detectability of biogeochemical impacts of ocean acidification (OA) on the marine alkalinity distribution from decadally repeated hydrographic measurements such as those produced by the Global Ship-Based Hydrographic Investigations Program (GO-SHIP). Detection of these impacts is complicated by alkalinity changes from variability and long-term trends in freshwater and organic matter cycling and ocean circulation. In our ensemble simulation, variability in freshwater cycling generates large changes in alkalinity that obscure the changes of interest and prevent the attribution of observed alkalinity redistribution to OA. These complications from freshwater cycling can be mostly avoided through salinity normalization of alkalinity. With the salinity-normalized alkalinity, modeled OA impacts are broadly detectable in the surface of the subtropical gyres by 2030. Discrepancies between this finding and the finding of an earlier analysis suggest that these estimates are strongly sensitive to the patterns of calcium carbonate export simulated by the model. OA impacts are detectable later in the subpolar and equatorial regions due to slower responses of alkalinity to OA in these regions and greater seasonal equatorial alkalinity variability. OA impacts are detectable later at depth despite lower variability due to smaller rates of change and consistent measurement uncertainty.

1. Introduction

Ocean acidification (OA) is one of many changes linked to carbon dioxide (CO_2) emissions from mankind's activities. The term ocean acidification refers to the decreases in seawater pH and the changes in seawater chemistry resulting from the continued ocean uptake of approximately one quarter of anthropogenic CO_2 released each year [*Le Quéré et al.*, 2015]. A portion of the protons (H^+) released into seawater as pH decreases are neutralized by reaction with carbonate ion according to the net reaction (equation (1)):

$$H_2O + CO_{2(aq)} + CO_3^{2-} \Leftrightarrow 2HCO_3^- \quad (1)$$

This net reaction summarizes how absorbed CO_2 can combine with water (H_2O) and neutralize basic carbonate ion (CO_3^{2-}) into bicarbonate ion (HCO_3^-). Decreasing CO_3^{2-} concentration disfavors calcium carbonate ($CaCO_3$) mineral formation. Earth System Models simulate ~50% surface CO_3^{2-} concentration reductions by 2100 under business-as-usual CO_2 emission scenarios [*Wolf-Gladrow et al.*, 1999; *Orr et al.*, 2005; *Bopp et al.*, 2013].

A critical question in OA research is how seawater chemistry changes will impact marine organisms. Many marine organisms use $CaCO_3$ to form shells and other hard parts, including organisms in the lower trophic levels of marine food webs (e.g., pteropods and coccolithopores), in key roles as ecosystem engineers (e.g., corals and calcifying algae), and that are fished and aquacultured commercially (e.g., clams and oysters). While it remains unclear how the entire ecosystems respond to OA-driven changes in seawater chemistry [*Pfister et al.*, 2014], laboratory and field studies suggest that the ability of organisms to form $CaCO_3$ hard parts is negatively impacted [e.g., *Orr et al.*, 2005; *Doney et al.*, 2009; *Bednaršek and Ohman*, 2015].

Total titration seawater alkalinity (A_T) is a convenient measurable seawater property for monitoring interactions between seawater chemistry and biological calcification. A_T is measured as the number of moles of strong acid required to bring seawater to a reference pH and can therefore be thought of as a measure of how well-buffered seawater is against pH changes. Each year, 0.5 to 1.6 Gt C is removed from the surface

ocean and exported to depth as biogenic $CaCO_3$, taking with it two moles A_T per mole carbon [*Dunne et al*., 2005, 2012b; *Berelson et al*., 2007]. This "hard tissue pump" in the pelagic ocean is the dominant factor responsible for the nearly global A_T increase with ocean depth (see *Carter et al*. [2014] for discussion of A_T measurements made prior to 2009). If we assume that the intensity of the hard tissue pump will be diminished by OA, then natural A_T depth gradients should relax, and changes in the A_T distribution from this relaxation should eventually become detectable. While the climate impacts of this A_T redistribution are not the focus of this study, we note this relaxation is a potentially significant negative feedback for anthropogenic CO_2 accumulation [*Doney et al*., 2009].

Here we ask how long it will take before a change in A_T distributions, measured decadally as part of the Global Ocean Ship-based Hydrographic Investigations Program (GO-SHIP), could be attributed to OA despite A_T measurement uncertainties and variability. *Ilyina et al*. [2009] answered this question using the global Hamburg Ocean Carbon Cycle Model to estimate OA-related A_T changes and decadal differences in measurements to estimate A_T variability. They estimated that alkalinity changes could become detectable after 2040. However, their fixed-circulation model was unable to resolve A_T changes from concurrent shifts in other processes such as ocean circulation, organic matter cycling, and freshwater cycling. Also, their globally uniform data-based A_T variability estimate prevented them from separately considering the various components of A_T variability or assessing how these components might vary regionally. In the present work, we aim to expand upon the Ilyina analysis by addressing these complications.

Biogenic $CaCO_3$ cycling is only the second most important control on the alkalinity distribution at the ocean surface, after freshwater cycling; alkalinity is diluted or concentrated when freshwater is added or removed, respectively [*Jiang et al*., 2014]. Intensification of the hydrological cycle is an expected consequence of global warming [*Held and Soden*, 2006] that has already been observed in surface salinity [*Durack et al*., 2012], so a detected A_T change as salty areas of the ocean get saltier and fresh areas of the ocean get fresher may have nothing to do with a biological response to OA. This challenges our ability to attribute A_T changes we detect to the biogeochemical consequences of OA. In addition, to be detected, a change must be larger than the background variability, and A_T variability from freshwater precipitation and evaporation is substantial. To a lesser extent than $CaCO_3$ cycling, organic matter cycling also affects seawater A_T through the exchange of protons during organic matter formation (proton uptake) and remineralization (proton release) [*Wolf-Gladrow et al*., 2007]. Changes to the hard and soft tissue pumps are another possible consequence of climate change, as changing circulation affects the return of micronutrients and macronutrients to the surface ocean [*Rost et al*., 2008] and the age distribution of deep waters. The model used by *Ilyina et al*. [2009] has fixed ocean circulation and freshwater cycling and is unable to resolve these potential changes.

Salinity normalizations and the idea of "potential A_T" (i.e., nitrate-adjusted A_T) have been long used to address the influence of freshwater and organic matter cycling, respectively, on A_T distributions [*Brewer et al*., 1975; *Rubin and Key*, 2002]. In this tradition, *Carter et al*. [2014] proposed Alk* as a tracer that isolates A_T variability owing to $CaCO_3$ cycling from the variability due to freshwater and organic matter cycling. Alk* is defined as follows:

$$\mathrm{Alk}^* = A_T + 1.26N - 66.4S \quad \mu\mathrm{mol\ kg}^{-1} \tag{2}$$

where Alk*, A_T, and N have units of μmol kg^{-1} and S is unitless. The added term with nitrate N accounts for the in situ A_T titration that occurs with organic matter remineralization, and the subtracted term with salinity S effects a salinity normalization. The constant 1.26 is based on an empirical relationship between calcium ion and nitrate found by *Kanamori and Ikegami* [1982], while the 66.4 constant is the volume-weighted mean surface A_T to S ratio [*Carter et al*., 2014]. Alk* has fewer sources of variability than A_T, potentially allowing a trend to be detected earlier and be more confidently attributed to OA versus other aspects of climate change. We test whether this is the case.

Internal variability is a complication that the constant-circulation model used by *Ilyina et al*. [2009] is unable to resolve. Internal variability refers to natural fluctuations in heat and freshwater budgets and ocean circulation that occur over a range of spatial and temporal scales, including everything from mixing over hours to days to large-scale synoptic storm events in the atmosphere to large-scale climate modes of variability (e.g., El Niño Southern Oscillation, or ENSO) [*Frölicher et al*., 2009; *Rodgers et al*., 2015]. These oscillations are important for shaping ocean property distributions on the decadal timescales we are concerned with. While internal

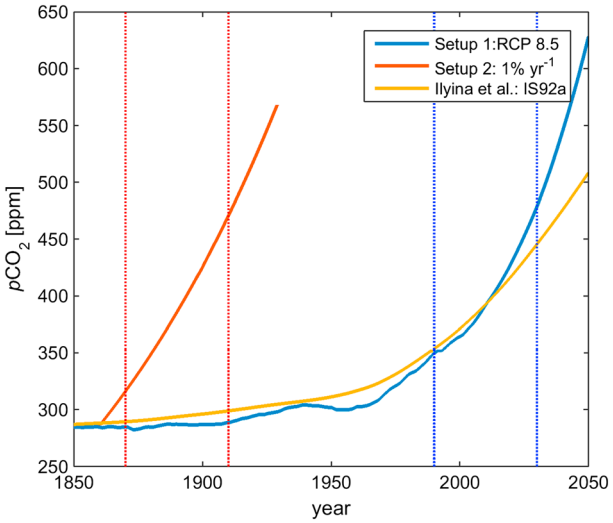

Figure 1. Atmospheric pCO_2 growth histories for our (blue) Setup 1 ensemble and (red) Setup 2 simulations. The vertical dotted lines indicate the time windows considered by our analysis. A (yellow) growth history estimated by *Joos et al.* [1996] for the IS92a emission scenario used by *Ilyina et al.* [2009] is provided for reference.

variability is a small barrier to detecting trends in rapidly changing pH [*Keller et al.*, 2014; *Rodgers et al.*, 2015], internal variability has not yet been thoroughly considered for A_T, which has a much smaller OA response compared to measurement precision than pH. The data-based variability estimate used by *Ilyina et al.* [2009] implicitly includes the effects of internal variability, but we argue that our novel ensemble approach provides a better internal variability estimate. This is because the Ilyina analysis only considers changes between two points in time along four hydrographic sections, while our ensemble approach allows us to estimate internal variability globally from 30 simulations of over 100+ years.

Finally, we question whether shallow depths are indeed the ideal place to look for decadal OA-related A_T changes. On decadal timescales, we expect surface trends to be larger than trends at depth because $CaCO_3$ formation is concentrated in the surface ocean while $CaCO_3$ dissolution is distributed across the broad deep ocean. However, variability complicating detecting A_T changes may be largest in the more dynamically active surface ocean (e.g. seasonal and interannual variability in evaporation and precipitation). We therefore also investigate whether trends from changes in pelagic calcification may be reasonably detected earlier at depth.

In summary, we aim to complement and expand upon the Ilyina analysis with several additional considerations:

1. We consider how freshwater, organic matter cycling, and circulation changes impact A_T distributions and may complicate interpretation of detected trends.
2. We test to what extent a salinity-normalized composite tracer such as Alk* [*Carter et al.*, 2014] could circumvent these additional complications or decrease the length of time required for detection of a trend.
3. We test the degree to which internal variability is an additional complication—beyond subdecadal variability and measurement uncertainty—and estimate internal variability from a large ensemble of simulations instead of hydrographic data.
4. We consider decadal chemistry changes at depth as well as at the surface.
5. We model with different assumptions as to drivers of $CaCO_3$ cycling.
6. We use an ensemble approach to characterize internal variability, which takes into account changes in the amplitude of major modes of variability over climate change timescales.

2. Methods

2.1. Model Simulations

We estimate A_T, nitrate (N), and salinity (S) concentration changes using the fully coupled carbon-climate Earth System Model ESM2M developed by the Geophysical Fluid Dynamics Laboratory (GFDL). The model consists of a 1° Modular Ocean Model version 4p1 (MOM4p1) MOM4p1 ocean version [*Griffies et al.*, 2009] coupled to a 2° version of the AM2 atmospheric model [*Anderson et al.*, 2004]. Ocean biogeochemistry is modeled with version 2 of the Tracers of Ocean Plankton with Allometric Zooplankton (TOPAZ2) biogeochemical package [*Dunne et al.*, 2013]. The control and experiment simulations diverge after more than 1000 years of physical and biogeochemical spin-up in the model year 1860 as described by *Dunne et al.* [2012a, 2013]. The experiment simulations then follow the historical atmospheric CO_2 and non-CO_2 greenhouse gas concentration pathway to 2005, and the high-emissions business-as-usual greenhouse gas Representative Concentration Pathway 8.5 (RCP8.5 [*Van Vuuren et al.*, 2011]) afterward (Figure 1).

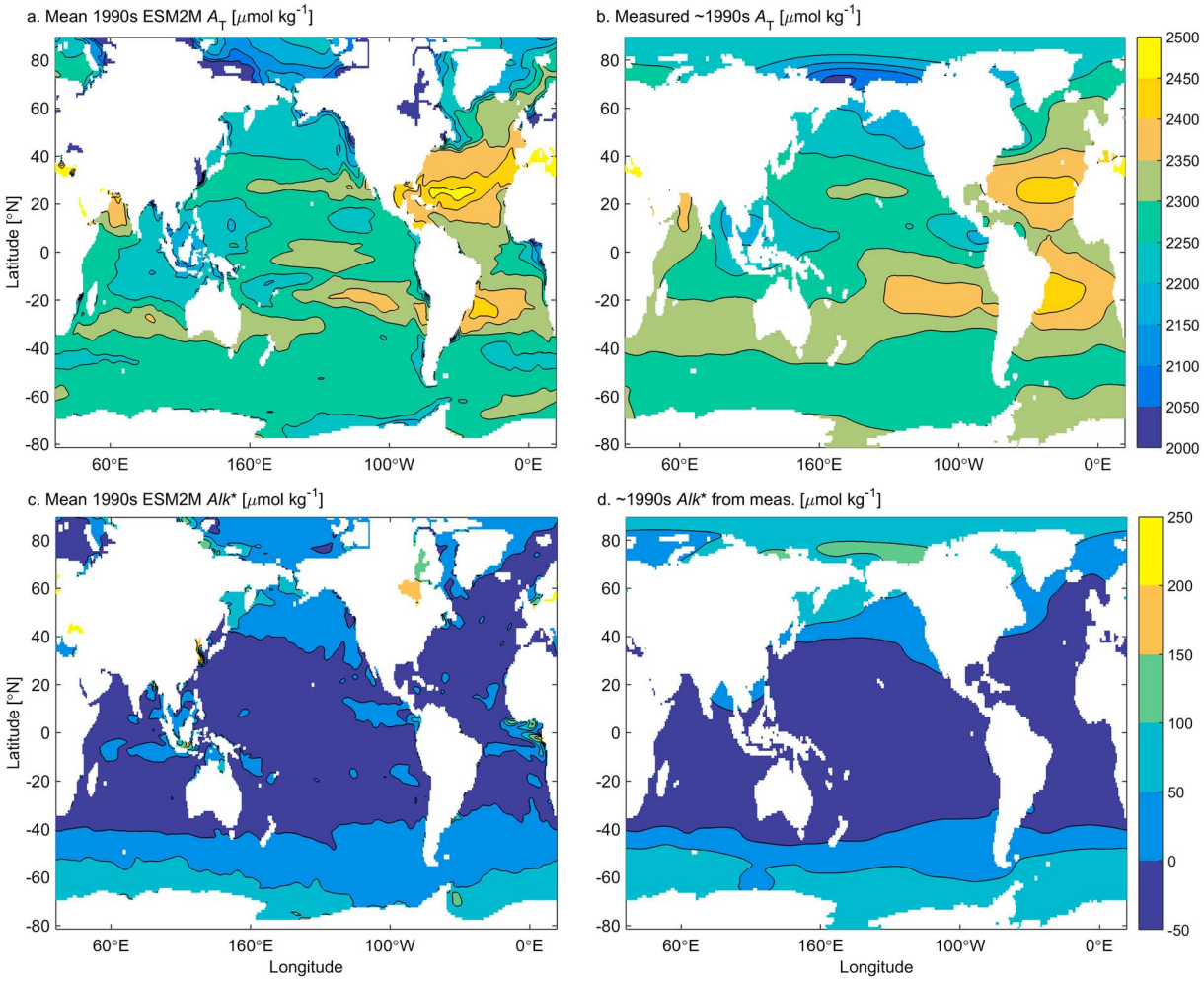

Figure 2. A comparison of (a) mean modeled A_T from the 1990s in the historical portion of the ESM2M simulation (Setup 1, ensemble member 1) to (b) the measured A_T distribution from 1970 to 2009 as compiled and gridded by *Carter et al.* [2014], and a comparison between mean Alk* inferred from (c) model outputs and (d) measurements.

We use a large initial condition ensemble suite with ESM2M to address timescales of emergence/detectability. With this approach the ensemble mean across all ensemble members represents the secular trend, while the individual ensemble members reveal a myriad of possible influences of internal variability. This approach has a longstanding history in weather prediction and climate dynamical studies and was first applied to ocean biogeochemistry by *Frölicher et al.* [2009]. Our 30 member ensemble of experiment simulations diverge from one another in model year 1950. The initial 1950 atmosphere/ocean/land/sea ice states for ensemble simulations 2 through 30 were taken from model state snapshots of the midnights of 1–29 January 1950 of ensemble simulation 1 [*Rodgers et al.*, 2015]. *Wittenberg et al.* [2014] showed that this is sufficient to randomize the ENSO index in this model within five model years. We begin consideration of trends starting with the 1990 introduction of Certified Reference Materials for A_T (which allow decadal A_T comparisons with quantifiable uncertainties) [*Dickson et al.*, 2003], so these ensemble members can be confidently assumed to have randomized internal states for our purposes. Tracer changes are expressed relative to changes in a single preindustrial control simulation with a constant atmospheric pCO_2 of 286 ppmv. Control simulation properties were smoothed using a 20 year running mean to minimize the influence of internal variability in this simulation. We refer to these simulations as the Setup 1-ensemble simulations and the Setup 1-control simulation. This model setup well captures the measured A_T and inferred Alk* distributions between 1990 and 2009 as described by *Millero et al.* [1998] and *Carter et al.* [2014], respectively (Figure 2). The model reproduces the strong correlations between A_T and S and between Alk* and phosphate concentrations observed in measurements. Like S, A_T is primarily controlled by

freshwater cycling, and like phosphate, Alk* is primarily controlled by biological cycling. The correlation coefficient between the measured and modeled A_T distributions in Figure 2 is 0.81 (versus 0.92 for Alk*). The largest disagreements in A_T and Alk* are in areas with strong influences from rivers (e.g., the Arctic Ocean) or upwelling (e.g., the Eastern Tropical Pacific and Atlantic). Given the strong correlations, the model likely adequately represents the dominant controls on the A_T and Alk* distributions for our purposes.

We use an additional pair of simulations with this model to identify the pattern of A_T changes that would be expected from OA alone (i.e., with an increase in atmospheric pCO_2, but without associated changes in ocean circulation and freshwater cycling due to climate change). The first of this pair is a 70 year control simulation with identical spin-up as used in Setup 1 and atmospheric CO_2 partial pressure held constant at 286 ppmv. The second is a simulation over the same time period with mixing and freshwater cycling forced to be identical to the control simulation, but with an atmospheric pCO_2 increasing at 1% per year for the final 70 years (Figure 1). This was accomplished by running two identical instances of the TOPAZ biogeochemistry model simultaneously in the ESM2M Earth system model. We call the year in which the control and experiment simulations diverge "year 1860." With identical ocean circulation, the A_T disparity that evolves over the 70 year experiment is attributable to biogeochemical OA feedbacks only. In this regard, this set of simulations is analogous to the simulation used in the Ilyina analysis. We also use the fixed 286 ppmv control simulation model to assess seasonal A_T and Alk* variability (because monthly outputs were most accessible from this simulation). We refer to these simulations as Setup 2-control simulation and Setup 2-experiment simulation.

Dunne et al. [2013]'s description of TOPAZ2 should be consulted for a full account of the biogeochemical model and its numerous potential feedbacks between climate and biogeochemical cycling, but we summarize the feedbacks most directly related to OA here. The TOPAZ2 biogeochemical package parameterizes three feedbacks between $CaCO_3$ cycling and the OA-sensitive $CaCO_3$ saturation state Ω, which is defined as follows:

$$\Omega = \frac{[Ca^{2+}][CO_3{}^{2-}]}{K_{sp\mathrm{CaCO_3}}} \tag{3}$$

$K_{sp\mathrm{CaCO_3}}$ is the temperature, salinity, and pressure-dependent solubility product specific to a given $CaCO_3$ mineral form (calcite or aragonite, for our purposes), calculated following the United Nations Educational, Scientific and Cultural Organization (UNESCO) 87 guidelines [*United Nations Educational, Scientific and Cultural Organization*, 1987]. $[CO_3{}^{2-}]$ and $[Ca^{2+}]$ are the concentrations of carbonate and calcium ions. Ca^{2+} concentrations are estimated as a function of salinity [*Riley and Tongudai*, 1967]. $CO_3{}^{2-}$ concentrations are calculated from prognostic A_T, total dissolved inorganic carbon C_T, S, and temperature T according to the procedure detailed by *Najjar and Orr* [1998]. OA decreases carbonate concentrations and therefore Ω. Decreasing Ω first impacts the TOPAZ2 parameterization for formation (and instantaneous export from the surface and dissolution at depth) of surface calcite detritus J_{CalcForm}. This formation rate is proportional ($\propto$) to the degree of calcite supersaturation (i.e., the degree to which the calcite saturation state $\Omega_{\mathrm{Calcite}}$ is > 1) and grazing on small plankton (e.g., coccolithophores) $J_{\mathrm{GrazSmall}}$:

$$J_{\mathrm{CalcForm}} \propto J_{\mathrm{GrazSmall}} \times \max(0, (\Omega_{\mathrm{Calcite}} - 1)) \tag{4}$$

A similar relationship is used for aragonite detritus formation from grazing on large phytoplankton (e.g., grazing by pteropods):

$$J_{\mathrm{AragForm}} \propto J_{\mathrm{GrazLarge}} \times \max\left(0, \left(\Omega_{\mathrm{Aragonite}} - 1\right)\right) \tag{5}$$

OA also impacts $CaCO_3$ dissolution in TOPAZ2, which is assumed to occur at a rate J_{Remin} proportional to the degree of undersaturation:

$$J_{\mathrm{CalcRemin}} \propto \max(0, (1 - \Omega_{\mathrm{Calc}})) \tag{6}$$

$$J_{\mathrm{AragRemin}} \propto \max\left(0, \left(1 - \Omega_{\mathrm{Arag}}\right)\right) \tag{7}$$

TOPAZ2 therefore assumes that there is no water column carbonate dissolution above the carbonate saturation horizon. Finally, Ω affects the fraction of $CaCO_3$ detritus reaching the ocean-sediment interface that is

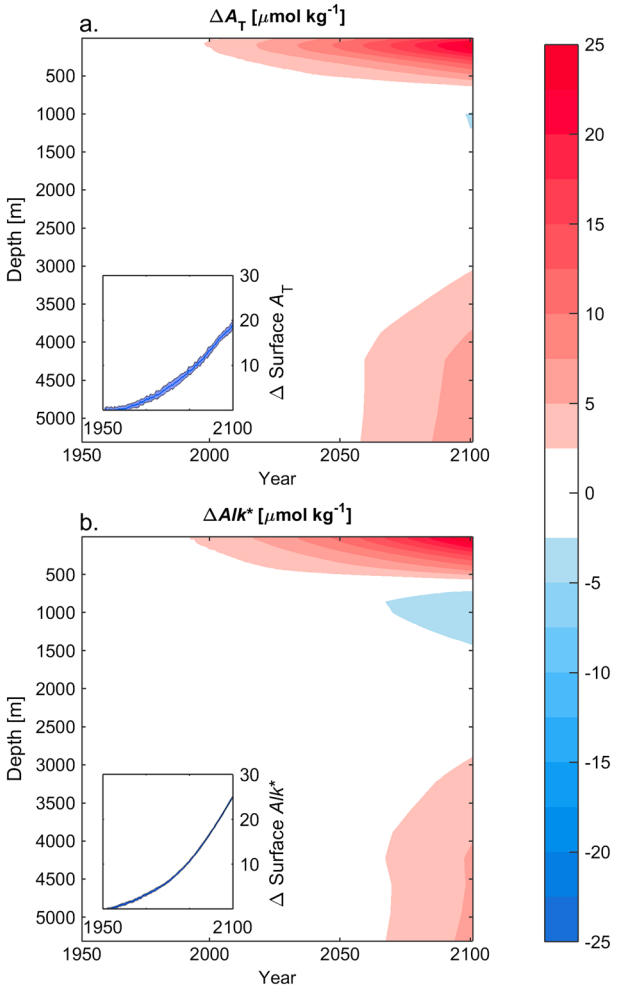

Figure 3. A Hovmöller diagram showing global ensemble mean surface to depth (a) A_T and (b) *Alk** anomalies (relative to the mean concentrations from 1950 to 1959) minus control anomalies against time in the simulation one-ensemble mean. Inset plots show the surface anomalies for the same time span, and narrow blue-grey windows around the lines on the inset plots indicate ensemble member standard deviations. The fact that these windows are barely visible highlights the high signal-to-noise ratio for globally integrated changes versus depth.

permanently buried. The fraction buried is determined by a combination of Ω and $CaCO_3$, organic, and lithogenic flux after *Dunne et al*. [2012b]. These are the three feedbacks in TOPAZ2 most directly related to the impact of OA on A_T and Alk* distributions.

The signal we are interested in detecting is the net effect of OA feedbacks on the A_T distribution (Figure 3). Surface A_T and Alk* increases occur when less A_T is exported from the surface in the form of $CaCO_3$. At middepths (750–2500 m), less $CaCO_3$ is dissolved due to the decreased surface export, leading to slight net A_T and Alk* decreases. Finally, small A_T increases occur at great depth. The deep increase primarily results from enhanced $CaCO_3$ dissolution in the water column and a slowdown of deep ocean overturning. *Ilyina and Zeebe* [2012] showed that changes from sedimentary interactions become large over centuries to millennia, though these changes remain small on the decadal timescales we are concerned with. Depth mean A_T and Alk* changes in Figure 3 are similar because freshwater cycling intensification primarily redistributes freshwater and alkalinity at the surface and does not strongly affect the mean surface value. However, the mean A_T increase is smaller at the surface than at 100 m depth, while the reverse is true for Alk*. This is because freshwater content is increasing at the surface and decreasing from 100 to 1000 m depth, likely due to decreased freshwater incorporation into mode and intermediate waters. Mean surface nutrient concentration decreases have a very small impact on mean surface A_T, peaking in 2100 with A_T increases of ~0.5 μmol kg^{-1}.

2.2. Signal, Noise, and Trend Detection

Trend detection involves distinguishing the target signal (a secular trend) from noise. Our signal is the influence of the secular trend in OA on A_T and the noise is both measurement uncertainty and natural variability on timescales longer than the approximately month-long repeat hydrographic cruises. We estimate both the signal and the noise from Earth system model simulations. Researchers have used coupled models to estimate noise for studies of the detectability of other Earth System trends. For example, *Deser et al*. [2014] and *Keller et al*. [2014] both considered trend emergence from noisy signals, but *Keller et al*. [2014] chose a definition of noise that was focused on interannual variations, whereas *Deser et al*. [2014] defined noise using the standard deviations of decadal trends from their large initial condition ensemble suite of runs. Our definition of noise is closer to that of *Keller et al*. [2014], given that, for our problem, seasonal and interannual variabilities have a large influence on the A_T distribution (discussed in section 3.3), but a small influence on

the pH changes driving OA-related A_T redistribution (when compared to anthropogenic CO_2 uptake) [*Rodgers et al*., 2015]. The effects of OA on the A_T distribution will therefore be more consistent between possible future states of the Earth system than the effects of other non-OA sources of interannual variability on A_T, and seasonal and interannual variabilities therefore are not noise in our signal of interest.

We define the target signal by fitting a second-order polynomial to Setup 1 ensemble mean A_T and Alk* from 1990 to 2050 in each grid cell using the number of years since 1990 (y) as our independent variable:

$$A_T(y) = Ay^2 + By + C \tag{8}$$

We use a second-order polynomial to allow for an accelerating or decelerating signal but note that all of our conclusions apply equally well when the analysis is done using linear fits over variable windows of time. We permit the added complexity of the second-order polynomials relative to linear fits because the linear fits change depending on the window of time considered, suggesting that the simpler model is inadequate to capture the response. We then use these polynomials to estimate the magnitude of the signal, or the ensemble mean property distribution changes (Δ's) over the years following 1990, by subtracting $A_T(0)$, which results in the following:

$$\Delta_{1990+y} = Ay^2 + By \tag{9}$$

Subscripts and superscripts for Δ estimates (e.g. $\Delta^{Alk^*}_{2030}$) indicate the calendar year and the property the estimate refers to, respectively. We also estimate polynomials in this manner for S and N, so we may later discuss changes in these properties (Δ^S and Δ^N) as they relate to changes in the A_T and Alk* distributions.

We estimate internal variability component of noise ($V_{Internal}$, with units of $\mu mol\, A_T\, kg^{-1}$) in two steps. First, we determine the standard deviation of annual mean A_T and Alk* between Setup 1 ensemble members for each of the years between 1990 and 2030 for each model grid cell. We then average these 40 standard deviation sets.

We estimate the seasonal variability component of noise ($V_{Seasonal}$, with units of $\mu mol\, A_T\, kg^{-1}$) as the standard deviation of the detrended monthly model outputs from the Setup 2-control simulation. We estimate $V_{Seasonal}$ separately for each year in the 10 year period from 1960 to 1970 to avoid including interannual variability (i.e., internal variability) in this estimate. We then average the 10 estimates for our combined seasonal variability estimate. We limit this analysis to a 10 year period due to computational constraints associated with monthly data.

We use 5 $\mu mol\, kg^{-1}$ as our estimate for the measurement uncertainty component of noise ($U_{Measurement}$). This estimate is for the most highly quality controlled alkalinity measurements currently attainable. This uncertainty was estimated as 6 $\mu mol\, kg^{-1}$ for the PACIFICA data set by *Suzuki et al*. [2013] and 3.3 $\mu mol\, kg^{-1}$ for the CARINA data set by *Velo et al*. [2009].

We do not separately estimate mesoscale variability or daily variations because averaging changes along hydrographic sections measured across months and many mesoscale variability length scales implicitly diminishes the influences of these kinds of variability.

We define the overall noise by combining $V_{Internal}$, $V_{Seasonal}$, and $U_{Measurement}$ added in quadrature. We refer to this combination of the variability and uncertainty terms as the noise "THRESHOLD," since changes must be greater than this value to be detected:

$$\sqrt{U_{Measurement}{}^2 + V_{Seasonal}{}^2 + V_{Interannual}{}^2} \equiv \text{THRESHOLD} \tag{10}$$

Equation (9) and our change detection criteria suggest a change is first detectable when:

$$\left|A_y{}^2 + B_y\right| > \text{THRESHOLD} \tag{11}$$

We are able to solve this equation for y when the response equals the THRESHOLD using the quadratic formula for each model grid cell, though we must solve it also with a negative THRESHOLD to allow for possible property decreases. Our "year of earliest detection" (YED) estimate is then anytime after the smallest positive real solution for y added to the year 1990.

YED estimates presume that the region was measured in 1990 using Certified Reference Materials and decadally since. They should be lengthened accordingly for regions where there were not World Ocean Circulation Experiment [*WOCE International Project Office*, 2003] quality measurements in the early 1990s. Also, it should be noted that the first batches of reference materials were certified for A_T retroactively, so 1990 may be too early of a reference year. Because our YED estimates are similar when assuming a linear response, our YED estimates can be adjusted for regions where high-quality measurements were first made after 1990 by simply adding the length of time between 1990 and when the region was first measured.

2.3. Validating THRESHOLD Estimates

We compare our THRESHOLD estimates derived from model variability to a data-based THRESHOLD estimate from measurements at A Long-term Oligotrophic Habitat Assessment (station AHOLA) and the Bermuda Atlantic Time-series Study (BATS). $V_{\text{Interannual}}$ is re-estimated for this analysis for the period over which measurements have been made at these stations. The BATS and ALOHA time series contain over 300 vertical A_T, S, and N profiles each measured since 1988 and 1993, respectively [*Joyce and Robbins*, 1996; *Karl and Lukas*, 1996]. These profiles are subject to all three sources of variability and uncertainty that contribute to THRESHOLD as well as variability on longer and shorter time and space scales (see section 2.2), allowing us to estimate THRESHOLD directly from data. We do not use these estimates for our main analysis because they are only two representations of the possible outcomes of the combined modes of variability and therefore do not provide robust statistics. Nevertheless, we can compare the data based estimates to our model-based THRESHOLDs to determine whether the two estimates are indeed of similar magnitude.

For each profile at ALOHA and BATS, we interpolate the property measurements onto the 50 model depth surfaces using a cubic Hermite piecewise polynomial interpolation. *Key et al*. [2004] showed that large (4–15 μmol kg^{-1}) errors could be introduced by such an interpolation. To reduce the potential for this error, we eliminate any interpolations between data points that are more than $(25 + z/15)$ m depth apart, where z is the depth of the interpolated value. This requirement prevents us from making comparisons at BATS below 195 m depth. Our data-based THRESHOLD estimate is then the standard deviation of measurements at each interpolated depth level, which we compare to our model-derived THRESHOLD.

3. Results and Discussion

We first discuss how well our data-based and model-based THRESHOLD estimates agree at ocean stations ALOHA and BATS in section 3.1. We then present and discuss Δ estimates in section 3.2 and the V_{Seasonal} and V_{Internal} THRESHOLD components in section 3.3. YED estimates are presented and discussed in section 3.4.

3.1. THRESHOLD Comparisons

We compare our data-based THRESHOLD estimates at ocean station ALOHA and BATS to the average THRESHOLD estimates from model variability within the 20° latitude and longitude window around each station at each depth (Figure 4). Our findings are not strongly sensitive to the size of this window. Model-based THRESHOLD estimates (black line) are of similar magnitude to the data-based THRESHOLD estimates (red dots) and loosely capture the variability with depth. Average data-based A_T THRESHOLD values exceed model-based THRESHOLD values near 250 m depth at ALOHA (Figure 4a), while the reverse is true at BATS (Figure 4b). A_T THRESHOLD values from BATS are similar to the modeled seasonal variability (blue line) but lower than the internal variability estimates (green line). This could either be because the modeled internal variability is higher than the true internal variability at BATS, or simply because there was less internal variability over the measurement period at BATS than is typical. By contrast, Alk* model and data-based THRESHOLD estimates agree well at the surface at both stations suggesting the discrepancy in the modeled and experienced A_T variabilities is primarily the result of variability in evaporation and precipitation. At depth, model-based THRESHOLD estimates are larger than data-based estimates for both A_T and Alk*. We attribute this to the consistency of the equipment, methods, and quality control procedures used at ALOHA and note that our 5 μmol kg^{-1} measurement uncertainty estimate applies to collections of measurements made by different labs with different equipment. In summary, this comparison suggests that our model-based THRESHOLD estimates are of appropriate magnitude. However, the comparison also serves to caution that Earth System internal variability is statistically defined and that much larger or smaller changes are possible

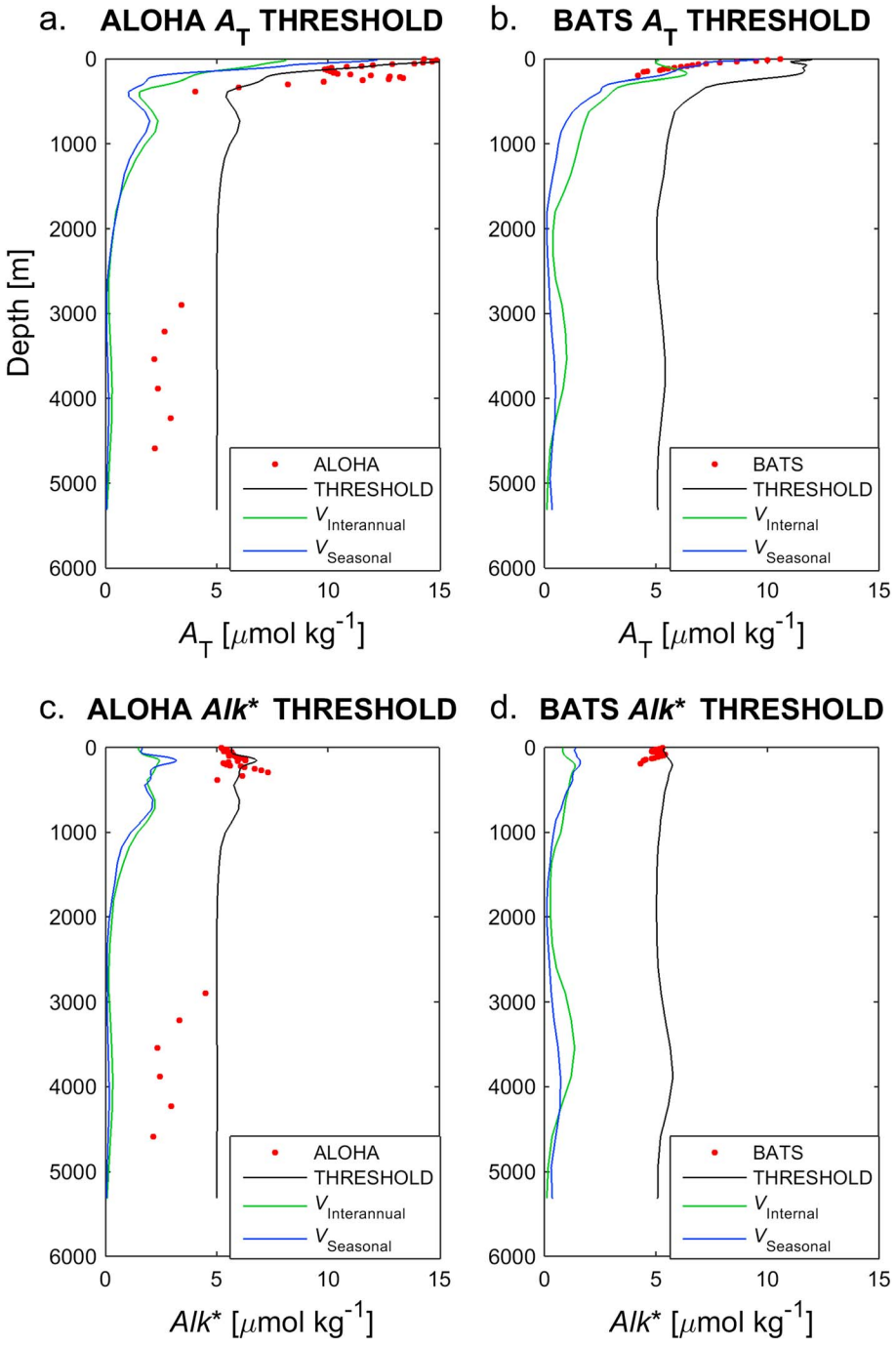

Figure 4. A comparison of model-based (black line) and data-based (red dots) THRESHOLD estimates against depth at ocean station (a, c) ALOHA and (b, d) BATS for (Figures 4a and 4b) A_T and (Figures 4c and 4d) Alk*. The $V_{Seasonal}$ (blue line) and $V_{Internal}$ (green line) contributions to THRESHOLD (see equation (10)) are plotted for reference.

within a given decadal window. Therefore, observed property changes should be both widespread and persistent before they can be attributed to long-term changes with confidence.

3.2. Trend Estimates

We first consider A_T change from model year 1870 to 1910 in the Setup 2 experiment (Figure 5). Observed A_T changes in Setup 2 are attributable to biogeochemical impacts because freshwater cycling and ocean circulation are held constant between the control and experimental simulations. We showed earlier (Figure 3) how

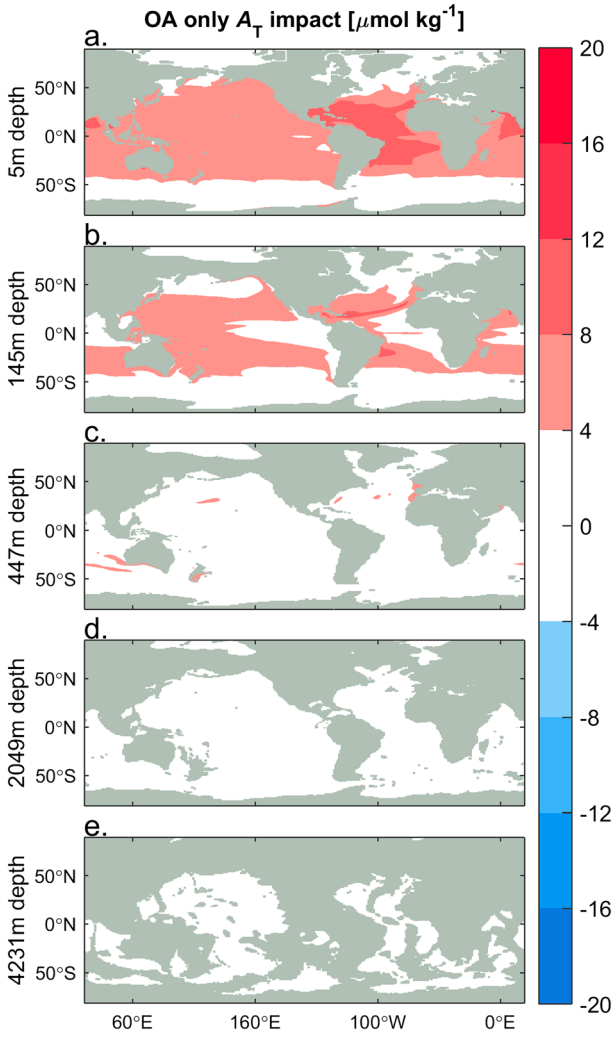

Figure 5. Maps of (a–e) A_T changes between model years 1870 and 1910 of the simulated 1% per year pCO_2 growth Setup 2 experiment (see Figure 1) at the five depth surfaces indicated on the left. Simulated A_T was adjusted by subtracting A_T in a control simulation with fixed atmospheric pCO_2 of 286 ppmv and identical circulation and freshwater cycling to the pCO_2 growth simulation. These changes therefore reflect only the influence of OA on the A_T distribution.

the Alk* distribution response to OA and climate changes varies with depth, and in Figure 5 we see the OA response also varies regionally as well. In the well-lit supersaturated ($\Omega > 1$) surface ocean, A_T accumulates with OA due to decreased $CaCO_3$ surface export. This is reflected in nearly universal positive surface and near-surface A_T changes (Figures 5a and 5b). OA-related surface A_T increases are smallest in the equatorial and Southern Ocean upwelling regions where seawater is more recently upwelled on average and has had less time to be affected by decreased $CaCO_3$ export. Patterns at depth (447+ m; Figures 5c–5e) reflect a balance between competing OA influences. Net A_T gains occur in comparatively well-ventilated regions (e.g., the subtropical gyre thermoclines and the subthermocline North Atlantic). Very small net A_T losses are found in deeper naturally corrosive waters that experience diminished $CaCO_3$ fluxes from the surface, but these changes are small enough as to appear white in our figures.

The patterns of modeled A_T changes we observe in our Setup 1 ensemble mean (Figure 6) are qualitatively similar to the A_T changes recently found by *Ilyina* [2015] using a version of the HAMOCC model that allows for hydrological cycle changes and is forced with historical and RCP8.5 CO_2 concentration pathways. A_T changes can be understood primarily as the combined effects of A_T redistribution from OA and intensification of the hydrological cycle. Ocean circulation and organic matter cycling changes have smaller influences. In the remainder of this section we consider the impact of each of these changes separately to account for Δ^{AT} values.

Alk* is formulated to be sensitive to ocean circulation and $CaCO_3$ cycling but not to freshwater or organic matter cycling. The broad similarity between $\Delta^{Alk^*}_{2030}$ values (Figure 6) and OA-related A_T changes (Figure 5) suggests that OA-related changes in $CaCO_3$ cycling are indeed the dominant factor responsible for Alk* changes. The $\Delta^{Alk^*}_{2030}$ values being slightly smaller than Setup 2 A_T changes despite the similar elapsed lengths of time is consistent with the faster atmospheric pCO_2 growth in the Setup 2 simulation. Similarities between $\Delta^{Alk^*}_{2030}$ and Δ^{AT}_{2030} values suggest that OA impacts can explain some of the A_T change. However, there are significant discrepancies between these distributions regionally that OA cannot account for.

Freshwater cycling changes are also significant for changes in A_T. Their influence can be estimated from salinity changes (Δ^{S}_{2030} in Figure 7). Freshwater dilutes both A_T and S linearly, so the influence of freshwater

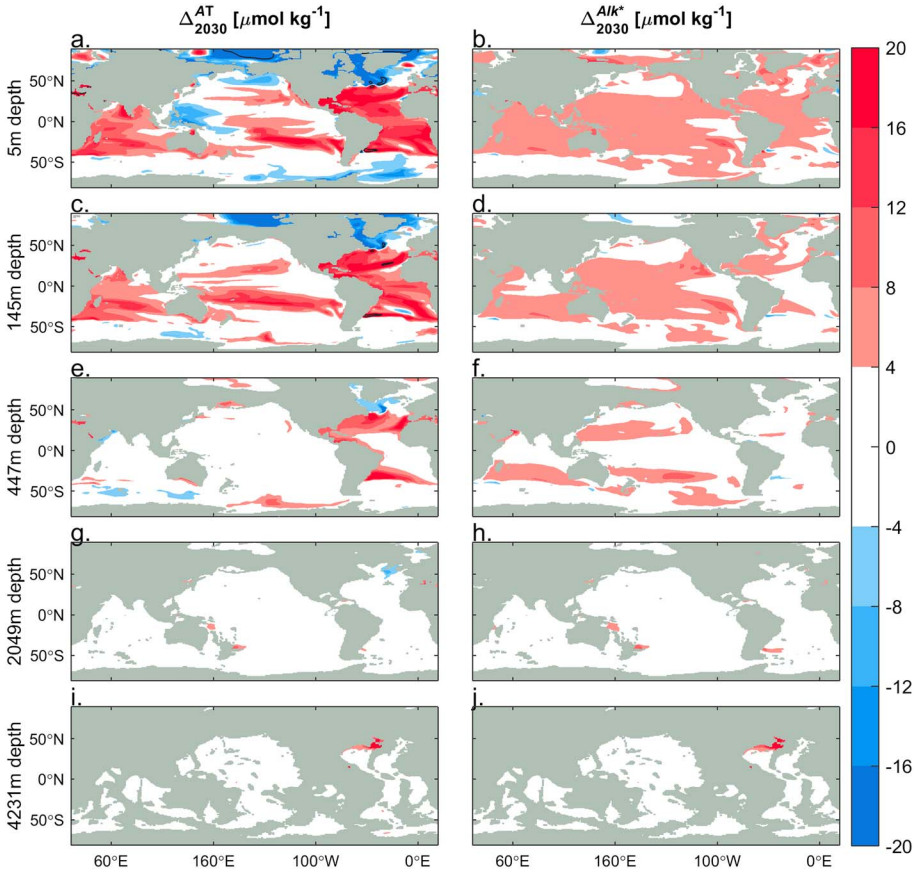

Figure 6. Maps of (a, c, e, g, and i) A_T and (b, d, f, h, and j) Alk* changes from 1990 to 2030 (Δ^{AT}_{2030} and $\Delta^{Alk^*}_{2030}$) in the Setup 1 ensemble mean at the five depth surfaces indicated on the left. We only plot Δ_{2030} values but note the distributions for other end dates are qualitatively similar. However, rates of change from 1990 to 2030 are generally larger than from 1990 to 2010 and smaller than from 1990 to 2050. Black contours encircle areas where values exceed colormap limits.

cycle changes on A_T can be approximated as the ratio of mean surface seawater A_T to S (~66.4 μmol kg^{-1} from measurements [*Carter et al.*, 2014] and ~66.2 in ESM2M) times the salinity change. The color scale for S changes in Figure 7 is set so the approximate A_T change expected to result from the S change shown equals the A_T change of the same color in Figure 6. This color scale obscures some of the largest changes, and 40 year salinity decreases of more than 1 are widespread across the Arctic and large increases are found at the boundary between the Subtropical Atlantic and the Southern Ocean. Freshwater cycling changes have a substantial impact on A_T changes. The largest changes in surface A_T are found in the rapidly freshening Arctic, Western Equatorial Pacific, and Southern Ocean, and the increasingly evaporative Atlantic and Indian Ocean. To a first approximation, A_T changes (Figure 6) can be seen to be the combination of Alk* changes (Figure 6) and S changes (Figure 7). This suggests that OA feedbacks and freshwater cycling changes collectively account for the majority of the Δ^{AT}_{2030} values.

A_T changes from changes in organic matter cycling are comparatively small. A_T changes in a −1:1 ratio with N in the TOPAZ2 biogeochemical model, so we expect the effect of changes in organic matter cycling on modeled A_T trends to equal the N changes. Figure 7 indicates that changes in N are generally less than 20% of the total A_T change.

N changes, like Alk* changes, can provide an indicator of ocean circulation or biogeochemical production changes. For example, bands of Alk* (and N) decreases near the Atlantic and Indian segments of the Southern Ocean Subtropical Front (Figures 6b, 6d, 7b, and 7d) that are not seen with fixed circulation (Figures 5a and 5b) are consistent with expansion of the low-Alk*, low-N, high-S subtropical gyres. Slowdown

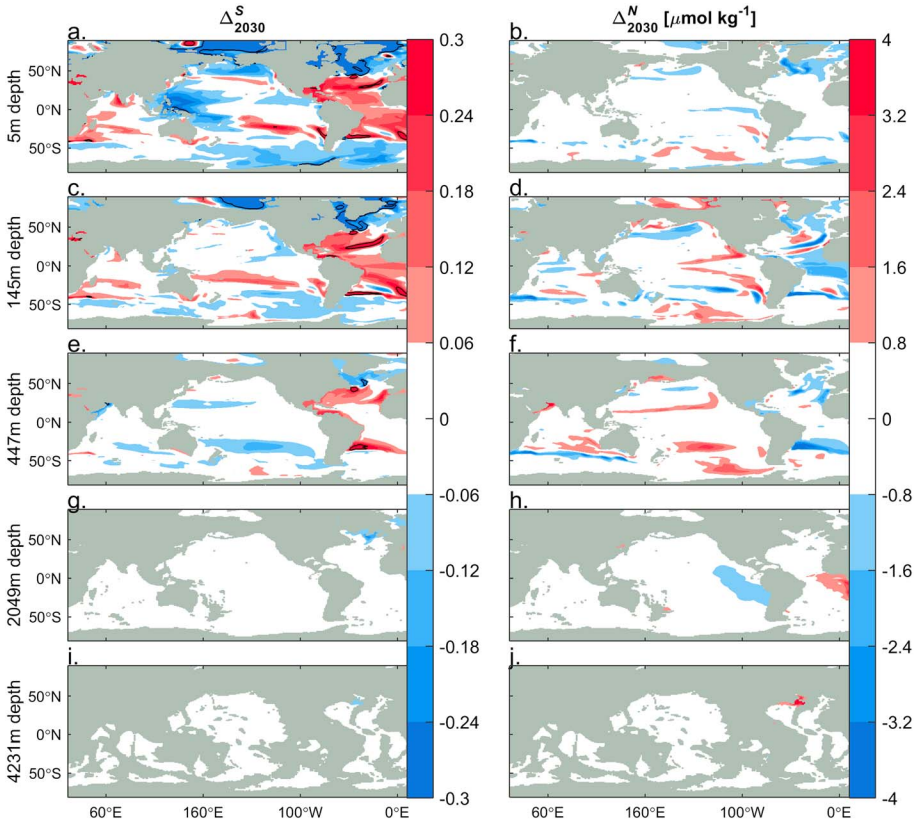

Figure 7. Maps of (a, c, e, g, and i) salinity (*S*) and (b, d, f, h, and j) nitrate (*N*) changes from 1990 to 2030 (Δ^{S}_{2030} and Δ^{N}_{2030}) in the Setup 1 ensemble mean at the depth surfaces indicated on the left. Contours encircle areas where values exceed colormap limits.

of the Atlantic Meridional Overturning Circulation can be seen in large increases in deep North Atlantic *N* and Alk* (Figures 6j and 7j) that are absent in fixed-circulation simulation Alk* changes (Figure 5e). Increasing Alk* and *N* are also both seen at 447 m depth (Figures 6 and 7) north of the Subtropical Mode Water (STMW) formation region in the Southern Pacific while similar large A_T increases are not seen with fixed circulation (Figure 5b). These changes are likely due to shifts in circulation, though whether to stagnation of the water mass at depth or increased contributions of upwelled high-Alk* high-*N* Upper Circumpolar Deep Water to STMW with increasing westerly wind strengths over the Southern Ocean is unclear. Nevertheless, the effects of circulation changes tend to be small or localized, and we expect them to be a minor cause for A_T changes compared to freshwater cycling and OA-related $CaCO_3$ changes outside of the mentioned regions.

3.3. Internal and Seasonal Variability

A_T internal variability (Figure 8) is large in the surface of the subtropical gyres, tropics, and Arctic. Internal variability is especially intense in the Western Pacific because of ENSO-related precipitation variability. ENSO-related internal variability is slightly overestimated by the ESM2M model we use [*Dunne et al.*, 2012a], so it is possible that this variability is an overestimate for some regions. Internal A_T variability decreases with increasing depth and is mostly smaller than our 5 μmol kg^{-1} measurement uncertainty estimate by 447 m depth. Surface internal variability in Alk* is substantially smaller than in A_T because the salinity normalization removes the effects of variability in evaporation and precipitation. The only places where Alk* internal variability is larger than our measurement uncertainty estimate are the Kuroshio Extension (where the boundary between the subpolar and subtropical gyres is highly variable) and the Arctic and the Bay of Bengal (where modeled riverine alkalinity inputs scale with variable land rainfall).

Seasonal A_T variability (Figures 9a, 9c, 9e, 9g, and 9i) is of comparable magnitude to internal variability for both properties. Seasonal variability is largest regionally in the highest and lowest latitudes due to large

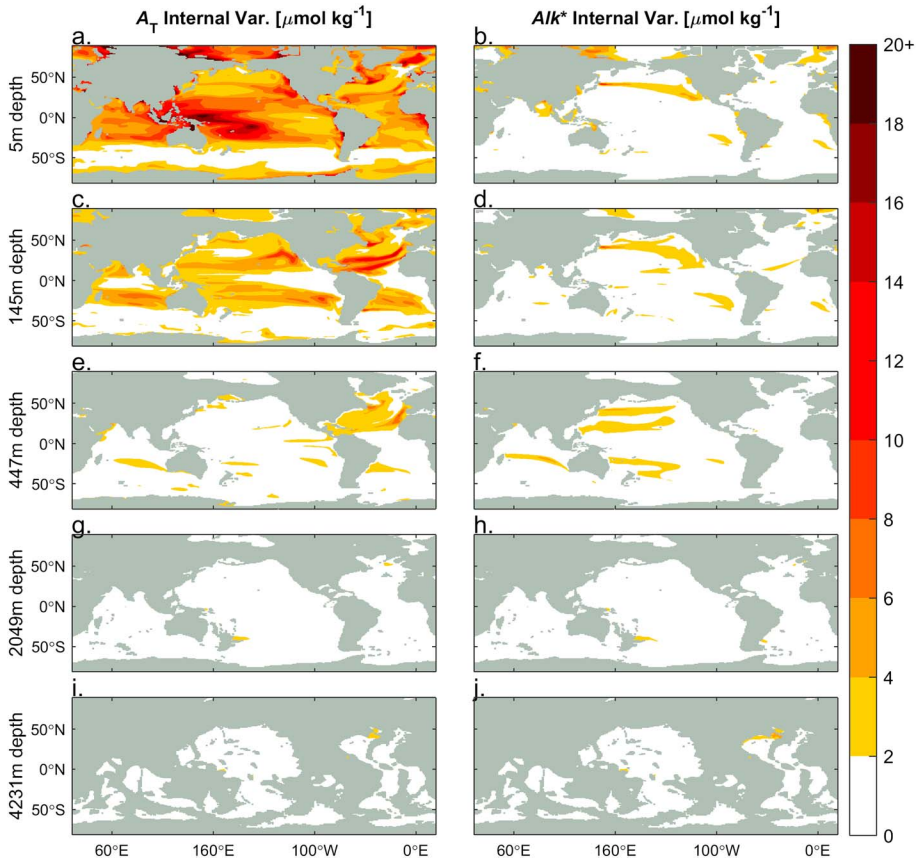

Figure 8. Maps of ensemble-based estimates of internal variability in (a, c, e, g, and i) A_T and (b, d, f, h, and j) Alk* for the depth surfaces indicated on the left for the years 1990 to 2050.

seasonal cycles in precipitation at these latitudes. The high latitudes also have large seasonal A_T cycles from sea ice formation and melting, as well as from riverine input variability in the Arctic. Seasonal Alk* variability (Figures 9b, 9d, 9f, 9h, and 9j) is generally lower than seasonal A_T variability. The largest seasonal Alk* variability is found at the surface in river plumes. This can be seen as high seasonal variability where the Ganges and Brahmaputra flow into the Bay of Bengal, at the mouths of the Congo and the Amazon Rivers, and broadly in the Arctic where numerous rivers empty (Figure 9). While Alk* is unaffected by freshwater cycling, river water can contain substantial A_T from dissolved minerals [*Cai et al*., 2008] that does affect Alk* [*Carter et al*., 2014].

Seasonal and interannual variabilities are significant considerations when searching for trends in decadal measurements. Both sources are in some places more than double the 9.8 μmol kg^{-1} variability threshold estimate applied globally by *Ilyina et al*. [2009]. They are a problem for such data-based estimates of THRESHOLD because they would require a long time series simply to accurately estimate the variability. Fortunately, Alk* removes the majority of seasonal and interannual variability by limiting the effects of variability in freshwater cycling.

3.4. Year of Earliest Trend Detections

YED estimates are the earliest years in which the A_T and Alk* changes exceed our THRESHOLD estimates and become "trends," though we again caution that what we call a trend is better thought of as a detectable change of low statistical significance. YED maps (Figure 10) suggest A_T and Alk* trends may already be detectable in some places. The earliest surface YED estimates are in the Arctic and Atlantic for A_T, though the Arctic YED values are underestimates given the lack of widespread 1990s measurements there. Surface Alk* YED estimates are earliest in the subtropical gyres. The subtropical gyres are likely where these changes are first detectable despite having low carbonate mineral export because these regions are exchanging water with

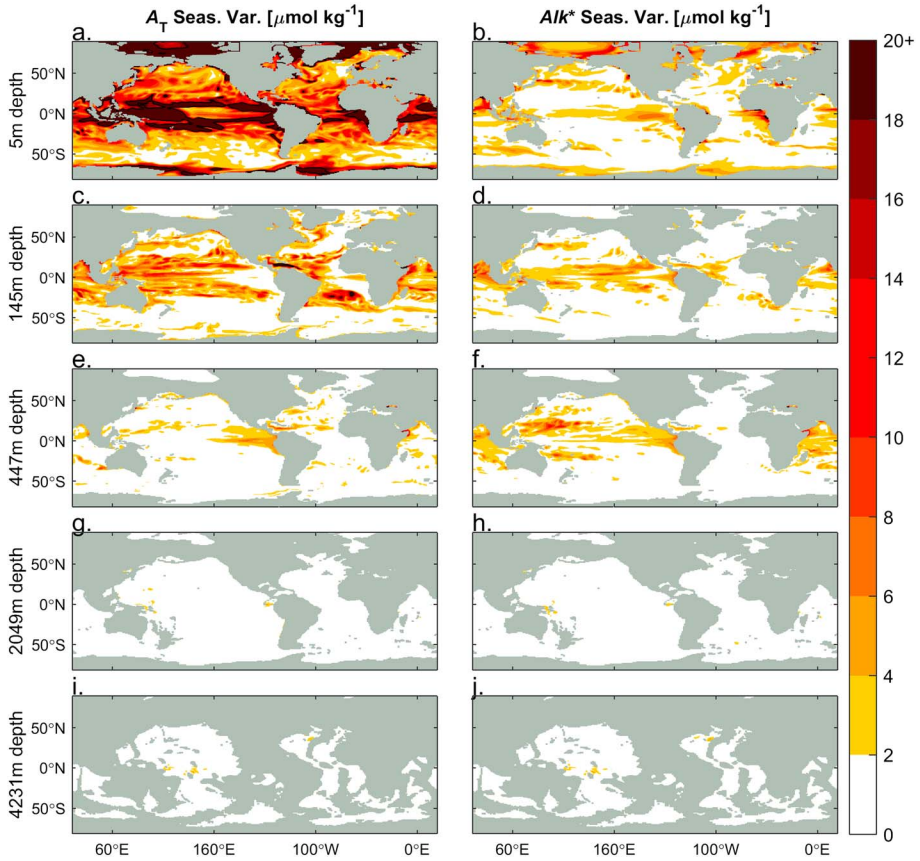

Figure 9. Maps of seasonal variability estimates (a, c, e, g, and i) A_T and (b, d, f, h, and j) Alk* for the depth surfaces indicated on the left in μmol kg^{-1}.

the more seasonally and interannually variable high- and low-latitude regions. The subtropics therefore experience comparable changes against a background of lower variability. Our simulations therefore suggest that a linear decline of calcification in response to saturation state changes with OA could be broadly detectable by 2030 across the surface of all subtropical gyres. However, *Ilyina et al*. [2009] show that the OA response is highly dependent on the assumed response of carbonate producing ecological communities to decreases in ocean Ω. While the model algorithms have some mechanistic justification, there is considerable variability in the carbonate production contribution to total biodiversity and its response to OA between models. The actual response is as yet poorly understood and highly uncertain, and so too is our estimate of 2030.

A clear caution for interpreting decadal measurement trends from Figure 10 is that some of the significant simulated A_T trends are unrelated to OA. This can be seen in the early (2010–2020) YED estimates across the Arctic and Atlantic for A_T (Figure 10a), which patterns of salinity change (Figure 7a) suggest are due rather to changes in patterns of evaporation, precipitation, and ice melt. Furthermore, OA-related A_T trends may be counteracted or obscured by evaporation and precipitation. An example of a A_T trend being obscured is the $>$2050 YED estimates across the North Pacific where there are $<$2030 YED estimates for Alk*. Using Alk* can eliminate this variability, allow a detected trend to be more confidently attributed to OA, and allow a trend to be detected earlier in some places. However, both A_T and Alk* can be redistributed by circulation changes. The YED estimates before 2020 below the surface are in many places partially the results of circulation changes—either directly through displacement of seawater by other seawater with a differing A_T and Alk* or indirectly through changes in modeled carbonate cycling patterns with nutrient redistributions—rather than OA. To support this claim, consider how the bands of early (2010–2020) Alk* YED estimates off the Californian Coast at 145 m depth, in the Southern Pacific Subtropical Gyre at 447 m depth, and in the deep

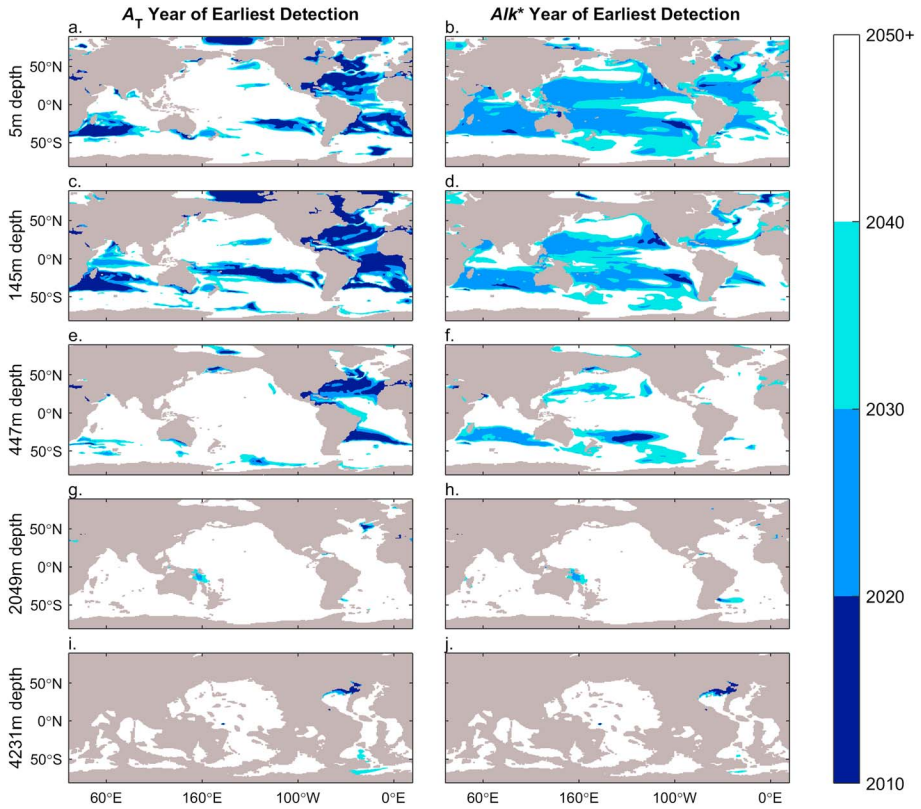

Figure 10. Maps of the year of earliest detection (YED) based on equation (11) for (a, c, e, g, and i) A_T and (b, d, f, h, and j) Alk*.

North Atlantic at 4231 m depth all coincide with positive *N* trends (Figure 7) and discrepancies between A_T changes under fixed circulation (Figure 5) and $\Delta^{Alk^*}_{2030}$ (Figure 6).

We can now answer a question we posed in section 1 regarding whether the intermediate or deep oceans are where we would expect the earliest detection of OA-related A_T trends, and the answer is no. Trends do become detectable at depths below 145 m, but in increasingly narrow regions at greater depth. Where Alk* trends are detectable, the trends appear to be the result of circulation changes rather than OA. The OA portion of the signal is generally detectable at a later date at greater depth due to smaller Δ values at depth. Compensating decreases in THRESHOLD are limited by a constant measurement uncertainty with depth.

How do our findings compare to *Ilyina et al.* [2009]'s? In their linear response simulation—the most comparable simulation to our own—*Ilyina et al.* [2009] find that A_T trends could be detectable by ~2010 in the Pacific Ocean, but not until 2040 in the Atlantic due to their smaller simulated preindustrial $CaCO_3$ production, and therefore, smaller OA-related A_T changes, in the Atlantic than in the Pacific. By contrast, we find that A_T trends would be detectable on this decade in large swaths of the Atlantic but not detectable until after 2050 in most of the Pacific because of complimentary and counteracting freshwater cycling-related A_T changes in the Atlantic and Pacific, respectively. Considering only the OA-related portion of the trend with Alk* trends, we still do not find that trends would be detected earlier in the Pacific than in other basins because, unlike their model, our model does not have larger initial $CaCO_3$ production (Figure 11) or a larger OA response in the Pacific than in the Atlantic (Figure 3). Slightly smaller seasonal and internal variability in the Atlantic and the Pacific is a secondary factor. The TOPAZ2 package simulates more $CaCO_3$ production along coasts, across the North Atlantic, and along the subtropical front of the Southern Ocean than the model used by the Ilyina study. *Ilyina et al.* [2009]'s model simulates substantially more $CaCO_3$ production in the equatorial Pacific. This discrepancy between our findings suggests that the baseline calcification patterns in the simulated preindustrial ocean are also important for regional detectability of OA trends. It should be noted that the RCP8.5

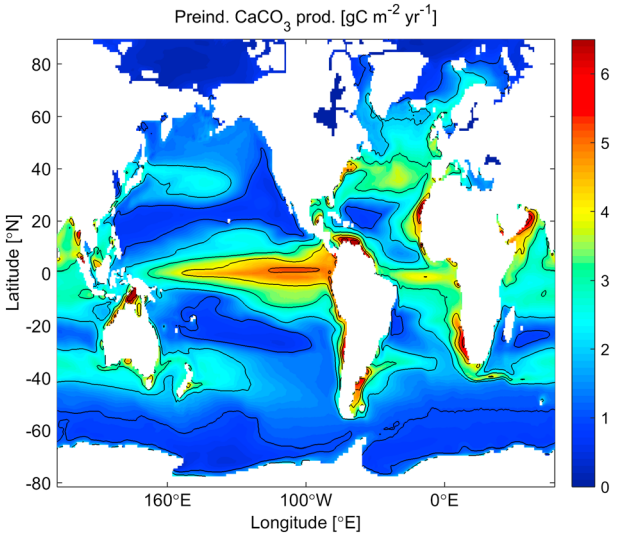

Figure 11. Map of preindustrial (model years 1860 to 1880 mean) $CaCO_3$ production in ESM2M with TOPAZ2. Contours are provided at intervals labeled on the color scale. The color scale for this figure is intended to be comparable to Figure 9a in *Ilyina et al*. [2009].

concentration pathway we use presumes greater emissions than the IS92a scenario used by *Ilyina et al*. [2009], with RCP8.5 emissions growing relative to IS92a from equal in the first years of this century to being ~50% greater in 2050 (see Figure 1 for a concentration pathway produced with IS92a). We therefore expect a greater OA response for a given ecological OA sensitivity in our simulations. However, atmospheric pCO_2 levels for the two scenarios are within 5 ppmv of one another from 1990 to 2015, so the earliest YED values should be comparable if this were the only difference.

4. Summary

We revisit the question first posed by *Ilyina et al*. [2009] of how long it will take before changes in the A_T distribution resulting from biogeochemical feedbacks with OA would be detectable. We use a comprehensive Earth System Model to simulate the A_T distribution response to climate changes that their simulations omitted—most notably freshwater and organic matter cycling and circulation changes—as well as to OA. We use a novel 30 member model ensemble to determine interannual variability as an additional complication for detecting trends from decadal data. We also extend the analysis to depth. We show the following:

1. Changes in freshwater cycling drive large changes in the A_T distribution that complicate interpretation of OA, posing a challenge to detecting the biogeochemical imprint of OA from A_T. These changes are so strong that they may already be detectable from repeat hydrographic A_T records.
2. There is yet considerable utility for decadal measurement for OA biogeochemical trend detection despite this complication: We argue that Alk* trends are unaffected by freshwater cycling trends, so detected *Alk** trends can be confidently assigned to OA provided circulation changes can be ruled out.
3. Surface A_T has substantial interannual and seasonal variability—up to several times measurement uncertainty—complicating A_T trend detection.
4. Alk* has less seasonal and interannual variabilities allowing trends to be separated from variability and measurement uncertainty earlier than trends in A_T in some regions.
5. Our modeled Alk* trends from OA would be broadly detectable across the subtropical gyres of the Indian, Pacific, and Atlantic by 2030 and in limited regions by 2020.
6. Estimates of when a trend could be detected appear sensitive to the simulated preindustrial distribution of $CaCO_3$ production.
7. OA-related trends would be detectable later at depth. This is because trend magnitudes (signal) and variability (noise) both decrease with depth, while measurement uncertainties (noise) remain constant. Furthermore, trends that are found at depth are more likely to be the result of shifts in ocean circulation rather than OA.

We caution here and elsewhere that our estimates for when a trend might be detectable presume an ecological response to OA that is yet poorly constrained, and are dependent on when high-quality A_T measurements first became available in a region. There are therefore large uncertainties on these estimates that are well documented and better constrained by the sensitivity analyses done by *Ilyina et al*. [2009], which showed that trends would become detectable 40+ years earlier or later with different ecological responses. Regardless of the exact ecological response, however, considering Alk* or salinity-normalized A_T changes will simplify interpretation and aid in detection of trends. Our analysis is consistent with and complementary to the Ilyina analysis in adding the six results noted above to the broader discussion.

Acknowledgments
We thank Swarthmore undergraduate researcher Jeong Do Ahn for his helpful explorations of carbonate cycling in ESM2M. Anonymous reviewers provided appreciated helpful feedback on the manuscript content and presentation. We are grateful to Kathy Tedesco of the Climate Observation Division of the NOAA Climate Program Office for funding for this research. B.R.C. was supported by the U.S. National Science Foundation (ANT-1040957) and the Carbon Data Management and Synthesis NOAA grant (N8R1SE3-PGC). T.L.F. acknowledges financial support from the SNSF (Ambizione grant PZ00P2_142573). The contribution of KBR came through awards NA17RJ2612 and NA08OAR4320752, which includes support through the NOAA Office of Climate Observations (OCO), and NOAA award NA11OAR4310066. ESM2M data output can be obtained from the Coupled Model Intercomparison Project data portal (http://cmippcmdi.llnl.gov/cmip5/data_portal.html), and the processed ensemble model output required to reproduce our figures is included as supporting information. This is PMEL contribution 4392 and JISAO contribution 2504.

References

Anderson, J. L., et al. (2004), The new GFDL global atmosphere and land model AM2-LM2: Evaluation with prescribed SST simulations, *J. Clim.*, *17*(24), 4641–4673.

Bednaršek, N., and M. Ohman (2015), Changes in pteropod distributions and shell dissolution across a frontal system in the California Current System, *Mar. Ecol. Prog. Ser.*, *523*, 93–103, doi:10.3354/meps11199.

Berelson, W. M., W. M. Balch, R. Najjar, R. A. Feely, C. Sabine, and K. Lee (2007), Relating estimates of $CaCO_3$ production, export, and dissolution in the water column to measurements of $CaCO_3$ rain into sediment traps and dissolution on the sea floor: A revised global carbonate budget, *Global Biogeochem. Cycles*, *21*, GB1024, doi:10.1029/2006GB002803.

Bopp, L., et al. (2013), Multiple stressors of ocean ecosystems in the 21st century: Projections with CMIP5 models, *Biogeosciences*, *10*(10), 6225–6245, doi:10.5194/bg-10-6225-2013.

Brewer, P. G., G. T. F. Wong, M. P. Bacon, and D. W. Spencer (1975), An oceanic calcium problem?, *Earth Planet. Sci. Lett.*, *26*(1), 81–87, doi:10.1016/0012-821X(75)90179-X.

Cai, W.-J., X. Guo, C.-T. A. Chen, M. Dai, L. Zhang, W. Zhai, S. E. Lohrenz, K. Yin, P. J. Harrison, and Y. Wang (2008), A comparative overview of weathering intensity and HCO^{3-} flux in the world's major rivers with emphasis on the Changjiang, Huanghe, Zhujiang (Pearl) and Mississippi Rivers, *Cont. Shelf Res.*, *28*(12), 1538–1549, doi:10.1016/j.csr.2007.10.014.

Carter, B. R., J. R. Toggweiler, R. M. Key, and J. L. Sarmiento (2014), Processes determining the marine alkalinity and calcium carbonate saturation state distributions, *Biogeosciences*, *11*(24), 7349–7362, doi:10.5194/bg-11-7349-2014.

Deser, C., A. S. Phillips, M. A. Alexander, and B. V. Smoliak (2014), Projecting North American climate over the next 50 years: Uncertainty due to internal variability, *J. Clim.*, *27*(6), 2271–2296, doi:10.1175/JCLI-D-13-00451.1.

Dickson, A. G., J. D. Afghan, and G. C. Anderson (2003), Reference materials for oceanic CO_2 analysis: A method for the certification of total alkalinity, *Mar. Chem.*, *80*(2–3), 185–197, doi:10.1016/S0304-4203(02)00133-0.

Doney, S. C., V. J. Fabry, R. A. Feely, and J. A. Kleypas (2009), Ocean acidification: The other CO_2 problem, *Annu. Rev. Mar. Sci.*, *1*, 169–192, doi:10.1146/annurev.marine.010908.163834.

Dunne, J. P., R. A. Armstrong, A. Gnanadesikan, and J. L. Sarmiento (2005), Empirical and mechanistic models for the particle export ratio, *Global Biogeochem. Cycles*, *19*, GB4026, doi:10.1029/2004GB002390.

Dunne, J. P., et al. (2012a), GFDL's ESM2 global coupled climate–carbon Earth System Models. Part I: Physical formulation and baseline simulation characteristics, *J. Clim.*, *25*(19), 6646–6665, doi:10.1175/JCLI-D-11-00560.1.

Dunne, J. P., B. Hales, and J. R. Toggweiler (2012b), Global calcite cycling constrained by sediment preservation controls, *Global Biogeochem. Cycles*, *26*, GB3023, doi:10.1029/2010GB003935.

Dunne, J. P., et al. (2013), GFDL's ESM2 global coupled climate–carbon Earth System Models. Part II: Carbon system formulation and baseline simulation characteristics, *J. Clim.*, *26*(7), 2247–2267, doi:10.1175/JCLI-D-12-00150.1.

Durack, P. J., S. E. Wijffels, and R. J. Matear (2012), Ocean salinities reveal strong global water cycle intensification during 1950 to 2000, *Science*, *336*(6080), 455–8, doi:10.1126/science.1212222.

Frölicher, T. L., F. Joos, G.-K. Plattner, M. Steinacher, and S. C. Doney (2009), Natural variability and anthropogenic trends in oceanic oxygen in a coupled carbon cycle-climate model ensemble, *Global Biogeochem. Cycles*, *23*, GB1003, doi:10.1029/2008GB003316.

Griffies, S., M. Schmidt, and M. Herzfeld (2009), *Elements of MOM4p1*, NOAA Geophysical Fluid Dynamics Laboratory, Princeton, N. J.

Held, I. M., and B. J. Soden (2006), Robust responses of the hydrological cycle to global warming, *J. Clim.*, *19*(21), 5686–5699, doi:10.1175/JCLI3990.1.

Ilyina, T. (2015), The combined effects of changes in ocean chemistry, biology, and hydrodynamics on alkalinity, *Nova Acta Leopold.*, *121*(408), 107–110.

Ilyina, T., and R. E. Zeebe (2012), Detection and projection of carbonate dissolution in the water column and deep-sea sediments due to ocean acidification, *Geophys. Res. Lett.*, *39*, L06606, doi:10.1029/2012GL051272.

Ilyina, T., R. E. Zeebe, E. Maier-Reimer, and C. Heinze (2009), Early detection of ocean acidification effects on marine calcification, *Global Biogeochem. Cycles*, *23*, GB1008, doi:10.1029/2008GB003278.

Jiang, Z.-P., T. Tyrrell, D. J. Hydes, M. Dai, and S. E. Hartman (2014), Variability of alkalinity and the alkalinity-salinity relationship in the tropical and subtropical surface ocean, *Global Biogeochem. Cycles*, *28*, 729–742, doi:10.1002/2013GB004678.

Joos, F., M. Bruno, R. Fink, U. Siegenthaler, T. F. Stocker, C. Le Quere, and J. L. Sarmiento (1996), An efficient and accurate representation of complex oceanic and biospheric models of anthropogenic carbon uptake, *Tellus, Ser. B*, *48*(3), 397–417, doi:10.1034/j.1600-0889.1996.t01-2-00006.x.

Joyce, T. M., and P. Robbins (1996), The long-term hydrographic record at Bermuda, *J. Clim.*, *9*(12), 3121–3131, doi:10.1175/1520-0442(1996)009<3121:TLTHRA>2.0.CO;2.

Kanamori, S., and H. Ikegami (1982), Calcium-alkalinity relationship in the North Pacific, *J. Oceanogr. Soc. Jpn.*, *38*(2), 57–62, doi:10.1007/BF02110291.

Karl, D. M., and R. Lukas (1996), The Hawaii Ocean Time-series (HOT) program: Background, rationale and field implementation, *Deep Sea Res., Part II*, *43*(2–3), 129–156, doi:10.1016/0967-0645(96)00005-7.

Keller, K. M., F. Joos, and C. C. Raible (2014), Time of emergence of trends in ocean biogeochemistry, *Biogeosciences*, *11*(13), 3647–3659, doi:10.5194/bg-11-3647-2014.

Key, R. M., A. Kozyr, C. L. Sabine, K. Lee, R. Wanninkhof, J. L. Bullister, R. A. Feely, F. J. Millero, C. Mordy, and T.-H. Peng (2004), A global ocean carbon climatology: Results from Global Data Analysis Project (GLODAP), *Global Biogeochem. Cycles*, *18*, GB4031, doi:10.1029/2004GB002247.

Le Quéré, C., R. Moriarty, R. M. Andrew, G. P. Peters, P. Ciais, P. Friedlingstein, and S. D. Jones (2015), Global carbon budget 2014, *Earth Syst. Sci. Data*, *7*(1), 47–85, doi:10.5194/essd-7-47-2015.

Millero, F. J., K. Lee, and M. Roche (1998), Distribution of alkalinity in the surface waters of the major oceans, *Mar. Chem.*, *60*(1–2), 111–130, doi:10.1016/S0304-4203(97)00084-4.

Najjar, R., and J. Orr (1998), Design of OCMIP-2 simulations of chlorofluorocarbons, the solubility pump and common biogeochemistry. [Available at http://www.ipsl.jussieu.fr/OCMIP/.]

Orr, J. C., et al. (2005), Anthropogenic ocean acidification over the twenty-first century and its impact on calcifying organisms, *Nature*, *437*(7059), 681–6, doi:10.1038/nature04095.

Pfister, C. A., et al. (2014), Detecting the unexpected: A research framework for ocean acidification, *Environ. Sci. Technol.*, *48*(17), 9982–9994, doi:10.1021/es501936p.

Riley, J. P., and M. Tongudai (1967), The major cation/chlorinity ratios in sea water, *Chem. Geol.*, *2*, 263–269, doi:10.1016/0009-2541(67)90026-5.

Rodgers, K., J. Lin, and T. Frölicher (2015), Emergence of multiple ocean ecosystem drivers in a large ensemble suite with an Earth system model, *Biogeosciences*, *12*, 3301–3320, doi:10.5194/bg-12-3301-2015.

Rost, B., I. Zondervan, and D. Wolf-Gladrow (2008), Sensitivity of phytoplankton to future changes in ocean carbonate chemistry: Current knowledge, contradictions and research directions, *Mar. Ecol. Prog. Ser.*, *373*, 227–237, doi:10.3354/meps07776.

Rubin, S., and R. Key (2002), Separating natural and bomb-produced radiocarbon in the ocean: The potential alkalinity method, *Global Biogeochem. Cycles*, *16*(4), 1105, doi:10.1029/2001GB001432.

Suzuki, T., et al. (2013), *PACIFICA Data Synthesis Project*, Carbon Dioxide Information Analysis Center, Oak Ridge National Laboratory, U.S. Department of Energy, Oak Ridge, Tenn.

United Nations Educational, Scientific and Cultural Organization (1987), *Thermodynamics of the Carbon Dioxide System in Seawater*, *UNESCO Tech. Pap. Mar. Sci.*, vol. 51, UNESCO, Paris.

Van Vuuren, D., J. Edmonds, and M. Kainuma (2011), The representative concentration pathways: An overview, *Clim. Change*, *109*(1), 5–31, doi:10.1007/s10584-011-0148-z.

Velo, A., F. F. Perez, P. Brown, T. Tanhua, U. Schuster, and R. M. Key (2009), CARINA alkalinity data in the Atlantic Ocean, *Earth Syst. Sci. Data*, *2*(1), 63–101, doi:10.5194/essdd-2-63-2009.

Wittenberg, A. T., A. Rosati, T. L. Delworth, G. A. Vecchi, and F. Zeng (2014), ENSO modulation: Is it decadally predictable?, *J. Clim.*, *27*(7), 2667–2681, doi:10.1175/JCLI-D-13-00577.1.

WOCE International Project Office (2003), WOCE observations 1990–1998; a summary of the WOCE global data resource, WOCE International Project Office, WOCE Report No. 179/02, Southampton, U. K.

Wolf-Gladrow, D. A., U. Riebesell, S. BurkHardt, and J. Bijma (1999), Direct effects of CO_2 concentration on growth and isotopic composition of marine plankton, *Tellus, Ser. B*, *51*(2), 461–476, doi:10.1034/j.1600-0889.1999.00023.x.

Wolf-Gladrow, D. A., R. E. Zeebe, C. Klaas, A. Körtzinger, and A. G. Dickson (2007), Total alkalinity: The explicit conservative expression and its application to biogeochemical processes, *Mar. Chem.*, *106*(1–2), 287–300, doi:10.1016/j.marchem.2007.01.006.